RE.PUBLIC@POLIMI

Research Publications at Politecnico di Milano

Post-Print

This is the accepted version of:

The final publication is available at http://dx.doi.org/10.1016/j.asr.2015.05.042

Access to the published version may require subscription.

When citing this work, cite the original published paper.

Analysis of Ballistic Capture in Sun–Planet Models

Z.-F. Luo[a], F. Topputo[b,*]

[a]*College of Aerospace Science and Engineering, National University of Defense Technology, 410073, Changsha, P. R. China*
[b]*Department of Aerospace Science and Technology, Politecnico di Milano, Via La Masa, 34, 20156, Milano, Italy*

Abstract

Analysis of ballistic capture orbits in Sun–plant systems is conducted in this paper. This mechanism utilizes purely gravitational forces, and may occur in non-Keplerian regimes. Ballistic capture orbits are generated by proper manipulation of sets of initial conditions that satisfy a simple definition of stability. Six Sun–planet systems are considered, including the inner planets, Jupiter, and Saturn. The role of planets orbital eccentricity, their true anomaly, and mass ratios is investigated. Moreover, the influence of the post-capture orbit in terms of inclination and orientation is also assessed. Analyses are performed from qualitative and quantitative perspective. The quality of capture orbits is measured by means of the stability index, whereas the capture ratio gives information on their statistical occurrence. Some underlying principles on the selection of the dynamical model, the initial true anomaly, and inclination are obtained. These provide a reference for practical cases.

Keywords: Ballistic capture, Stable sets, Restricted three-body problem

1. Introduction

Ballistic capture occurs when a particle switches from one dominant attractor to another, by virtue of a purely natural mechanism. This technique employs multibody dynamics to reduce the hyperbolic excess velocity upon approach, and therefore it cannot be reproduced in models implementing the classical Keplerian decomposition of the Solar System. In applications, the orbit insertion burn can be avoided if temporary capture by the target is acceptable. If not, a temporary capture orbit can

---

*Corresponding author.
 Email addresses:* `luozongfu200@nudt.edu.cn` (Z.-F. Luo), `francesco.topputo@polimi.it` (F. Topputo)

provide multiple opportunities for insertion into stable orbits, so mitigating the risks brought by single-point failures. Overall, ballistic capture is a promising technique that requires further analyses to increase our confidence.

In celestial mechanics, ballistic capture has been applied to study the natural capture phenomenon of asteroids, comets, and irregular satellites (Brunini, 1996; Neto and Winter, 2001; Astakhov et al., 2003; Lee et al., 2007). In astrodynamics, ballistic capture orbits have been used as insertion trajectories in lunar missions, such as in Hiten (Belbruno and Miller, 1993), SMART-1 (Schoenmaekers et al., 2001), and GRAIL (Chung et al., 2010). After these successful applications, ballistic capture has been proposed as baseline solution for missions to Mercury (Jehn et al., 2004), to the Moon (Elliot and Alkalai, 2011; Vetrisano et al., 2012), to the Jupiter moons (Alessi and Pergola, 2012; Campagnola et al., 2014), and in asteroid retrieval contexts (Urrutxua et al., 2014). More recently, ballistic capture has been employed to define a new paradigm for missions to Mars (Topputo and Belbruno, 2015).

Ballistic capture has been studied under the perspective of transit orbits about the Lagrange points (Conley, 1968; Yamato and Spencer, 2004; Circi, 2012) and invariant manifolds associated to the orbits around them (Koon et al., 2001; Gómez et al., 2001). Another approach consists in using the capture sets. These are sets of initial conditions that give rise to orbits satisfying a simple definition of stability (García and Gómez, 2007; Topputo and Belbruno, 2009; Sousa Silva and Terra, 2012). Capture sets are sets containing orbits that perform ballistic capture, and are defined by manipulation of the stable sets (Hyeraci and Topputo, 2010). This approach can be replicated in models incorporating planets eccentricity (Makó et al., 2010; Makó, 2014), fourth-body perturbations (Romagnoli and Circi, 2009), and full-ephemeris dynamics (Luo et al., 2014). Differences on capture orbits in the circular restricted three-body problem (CRTBP) and elliptic restricted three-body problem (ERTBP) have been observed in Hyeraci and Topputo (2010). The effect of the primaries true anomaly in the ERTBP has been studied in Circi and Teofilatto (2005); Prado and Neto (2006); Hyeraci and Topputo (2013); Makó (2014). The effect of perturbations has been analyzed in Machuy et al. (2007); Topputo (2013). Ballistic capture in the real system has been reproduced in Lei et al. (2013); Luo et al. (2014); Brasil et al. (2015).

Although some issues have been unveiled, a number of others are still open; e.g.,

1) It is known that the orbital eccentricity of the primaries affects the ballistic capture dynamics. However, it is not known to what extent the existence and distribution of ballistic capture orbits is influenced. Quantitatively, what is the effect of the primaries eccentricity over the capture sets?

2

2) Analyses in Circi (2012); Hyeraci and Topputo (2013); Makó (2014) show that the capture is facilitated when the primaries are about their perihelion. Does this behavior happen in general for any Sun–planet system? Is there a specific true anomaly that makes the capture more likely?

3) Capture sets are constructed by integrating post-capture periapsis conditions. However, the effect of the spatial distribution of these orbits is not completely understood. How does the orientation of the osculating plane affect the capture sets and the associated capture orbits?

The investigation conducted in the present work elaborates on the points above. In particular, three key aspects of ballistic capture are assessed, which involve studying 1) the role of the dynamical model, 2) the influence of the true anomaly, 3) the spatial distribution of the post-capture orbits. In this analysis, the capture sets are constructed with the algorithm in Luo et al. (2014) for six Sun–planet systems. Although in these cases the ballistic capture is mainly governed by a three-body dynamics, each system is simulated with three different models (CRTBP, ERTBP, full ephemeris model) having a well-defined hierarchy. This allows us to infer the role played by these models. Ad-hoc tools are developed to examine the results. The stability index provides information on the quality of the capture, whereas the capture ratio is a quantitative measure of the occurrence of capture. Both indexes are applied to the study cases developed, and critical analyses are made.

The reminder of the paper is organized as follows. Section 2 provides background notions. Section 3 describes the methodology in Luo et al. (2014), and introduces the stability index and capture ratio. An analysis of the simulations is performed in Section 4, where results are summarized. Section 5 contains concluding remarks.

2. Background

In the analysis below, the planet, of mass m_p, is the body around which the ballistic capture is studied. The mass ratio of a Sun–planet system is $\mu = m_p/(m_p + m_s)$, where m_s is the mass of the Sun. The physical parameters of the planets considered in this work are listed in Table 1.

2.1. Reference Frames

The planetary ephemerides are defined in the Earth mean equator and equinox of J2000 (EME2000 from now on). This frame, labelled (x_e, y_e, z_e), may be centered either at the Earth or at any other planet. Relative to this frame it is possible to define a planetocentric radial-tangential-normal frame at epoch t_0, (x_r, y_r, z_r),

3

Table 1: Parameters of target planets ([Russell, 2012](#)). R_s is the radius of the sphere of influence (SOI), whereas R is the mean equatorial radius.

Planet	Radius R, km	Mass ratio μ	Semi-major axis a, km	Eccent. e	SOI R_s, $\times R$
Mercury	2,439.7	1.660E-07	5.791E+07	0.2056	45.92
Venus	6,051.8	2.448E-06	1.082E+08	0.0068	101.80
Earth	6,371.0	3.003E-06	1.496E+08	0.0167	145.03
Mars	3,389.5	3.227E-07	2.279E+08	0.0934	170.00
Jupiter	69,911	9.537E-04	7.784E+08	0.0484	674.20
Saturn	58,232	2.857E-04	1.427E+09	0.0542	908.34

RTN@t_0 for brevity, by looking at the apparent motion of the Sun. The z_r-axis is perpendicular to plane of the Sun orbit, the x_r-axis is aligned with the Sun–planet line and points from the Sun to the planet, and the y_r-axis completes the dextral orthonormal triad (see Fig. 1). Note that the RTN@t_0 is a fixed frame.
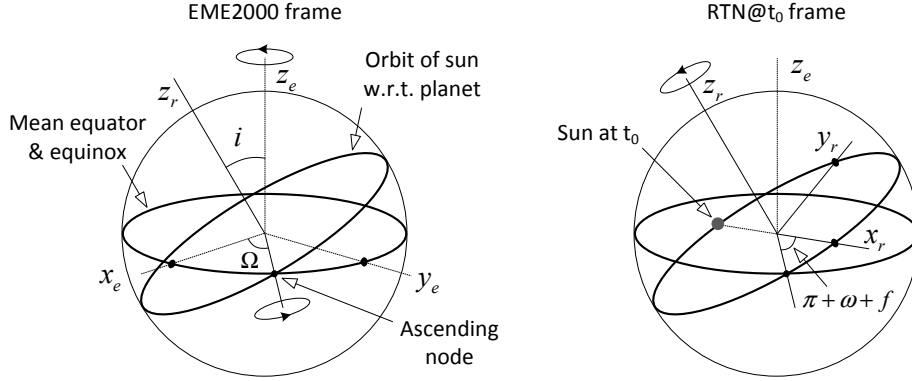
Figure 1: Geometry of EME2000 (left) and RTN@t_0 (right) frames.

Let i, Ω, ω, and f be the inclination, the right ascension of the ascending node (RAAN), the argument of periapsis, and the true anomaly of the Sun at epoch t_0 in the EME2000 frame, respectively. The transformation from RTN@t_0 to EME2000 can be obtained as the composition of three rotations, thus yielding

$$
\begin{pmatrix} x_e \\ y_e \\ z_e \end{pmatrix} = \begin{bmatrix} \text{s}\theta\ \text{s}\Omega\ \text{c}i - \text{c}\theta\ \text{c}\Omega & \text{s}\theta\ \text{c}\Omega + \text{c}\theta\ \text{s}\Omega\ \text{c}i & \text{s}\Omega\ \text{s}i \\ -\text{c}\theta\ \text{s}\Omega - \text{s}\theta\ \text{c}\Omega\ \text{c}i & \text{s}\theta\ \text{s}\Omega - \text{c}\theta\ \text{c}\Omega\ \text{c}i & -\text{c}\Omega\ \text{s}i \\ -\text{s}\theta\ \text{s}i & -\text{c}\theta\ \text{s}i & \text{c}i \end{bmatrix} \begin{pmatrix} x_r \\ y_r \\ z_r \end{pmatrix}, \quad (1)
$$

4

where $\theta = \omega + f$, and 's' and 'c' are used to abbreviate 'sin' and 'cos', respectively.

A barycentric pulsating rotating frame (BPR, for brevity), labelled (x, y, z), is used in ex post facto analyses. The origin of this frame is at the Sun–planet barycenter, the x-axis rotates with the line from the Sun to the planet, the z-axis is aligned with their orbital angular momentum, and the y-axis completes the triad; the Sun–planet distance is always set to unity. The definition of this frame is not attached to an epoch (as in EME2000 and RTN@t_0) since the axes and scalings are continuously adjusted to match the definition above. In this way, the Sun and planet are located at $(-\mu, 0, 0)$ and $(1 - \mu, 0, 0)$, respectively (Szebehely, 1967).

2.2. Dynamical Models

The equations of motion for a particle in the restricted n-body problem are

$$\ddot{\mathbf{r}} + \frac{\mu_p}{r^3}\mathbf{r} + \mu_s \left(\frac{\mathbf{r}_s}{r_s^3} + \frac{\mathbf{r} - \mathbf{r}_s}{\|\mathbf{r} - \mathbf{r}_s\|^3} \right) = -\sum_{i \in \mathbb{P}} \mu_i \left(\frac{\mathbf{r}_i}{r_i^3} + \frac{\mathbf{r} - \mathbf{r}_i}{\|\mathbf{r} - \mathbf{r}_i\|^3} \right), \qquad (2)$$

where μ_p and μ_s are the gravitational constants of the planet and the Sun, and $\mathbf{r}$ and $\mathbf{r}_s$ are the position vectors of the spacecraft and the Sun, respectively. Equation (2) is written in the EME2000 frame centered at the planet. The right-hand side accounts for fourth-body perturbations; $\mathbb{P}$ is a set containing the perturbing bodies, μ_i are their gravitational constants, and $\mathbf{r}_i$ are their position vectors.

In the full-ephemeris model (EPHE from now on) the states of the Sun and planets are extracted from the JPL DE430 model (Folkner et al., 2014). The SPICE toolkit is used to read the ephemerides, which is publicly available[1]. The ERTBP is obtained from (2) by setting $\mathbb{P} = \emptyset$ (which zeroes the right-hand side) and by computing $\mathbf{r}_s(t)$ through Eq. (1) as

$$\mathbf{r}_s(t) = -\frac{a(1 - e^2)}{1 + e \cos f(t)} \begin{pmatrix} s\theta \ s\Omega \ ci - c\theta \ c\Omega \\ -c\theta \ s\Omega - s\theta \ c\Omega \ ci \\ -s\theta \ si \end{pmatrix}, \qquad (3)$$

where a and e are the semi-major axis and the eccentricity of the orbit of the planet. The orbital parameters in (3) are read at initial time and kept constant during the simulation, except for the true anomaly f, which is computed by solving Kepler's equation at each time step. The CRTBP is obtained as a special case of the ERTBP by setting $e = 0$ in Eq. (3).

---

[1] http://naif.jpl.nasa.gov/naif/toolkit.html

2.3. Numerical Integration

Equations (2) are integrated numerically. Integrating these equations over those written in rotating frames allows us 1) tracking the authentic number of revolutions, in place of spurious counts, as in Hyeraci and Topputo (2010)); 2) computing conveniently the Kepler energy, so avoiding complex derivations as in Makó et al. (2010); Makó (2014)); 3) comparing directly the orbits in the three models, with no need of post-processing.

In order to speed-up the integration and avoid ill-conditioned problems, Eqs. (2) are normalized by using the units in Table 2 and the physical parameters in Table 1. A Runge–Kutta–Felhberg $7^{\text{th}}/8^{\text{th}}$ order integration scheme with relative and absolute tolerances set to 10^{-12} is used to numerically propagated initial conditions.

Table 2: Normalized units.

Symbol	Remark	Unit	Comment
MU	Gravity parameter unit	km^3/s^2	Planet gravitational parameter
LU	Length unit	km	Planet mean radius
TU	Time unit	s	$\sqrt{(LU^3/MU)}$
VU	Velocity unit	km/s	LU/TU

3. Methodology

The algorithm developed in Luo et al. (2014) is used to construct ballistic capture orbits. This approach extends the results in Belbruno (2004); García and Gómez (2007); Topputo and Belbruno (2009) to the spatial case. For the sake of completeness, the construction method is briefly presented below.

3.1. Classification of Orbits

The particle motion is classified according to geometrical and energetic arguments. To this aim, a semi-plane is introduced to count the revolutions of the particle around the planet (the dark grey plane in Fig. 2(a)). Let $\mathbf{r}_0$ and $\mathbf{v}_0$ be the particle initial position and velocity in the EME2000 frame centered at the planet, and let $\mathbf{r}(t)$ and $\mathbf{v}(t)$ be the same quantities at a subsequent (or previous) time t. Let also $\mathbf{h}_0 = \mathbf{r}_0 \times \mathbf{v}_0$ be the initial angular momentum. The particle lies on the intersection plane when $\mathbf{r}(t) \cdot (\mathbf{h}_0 \times \mathbf{r}_0) = 0$.

6

Remark 1 (Revolution). *The particle performs a complete revolution around the planet at time t_1 if the following conditions are all simultaneously satisfied,*

$$\mathbf{r}^{(k)}(t_1) \cdot (\mathbf{h}_0 \times \mathbf{r}_0) = 0, \qquad \mathbf{r}^{(k)}(t_1) \cdot \mathbf{r}_0 > 0, \qquad \left(\mathbf{v}^{(k)}(t_1) \cdot \mathbf{v}_0\right)\left(\mathbf{v}^{(k-1)} \cdot \mathbf{v}_0\right) > 0, \quad (4)$$

where the superscript (k) counts the number of intersections between the plane and the orbit (see Luo et al. (2014) for details).

(a) Intersection plane (b) Orbit categories
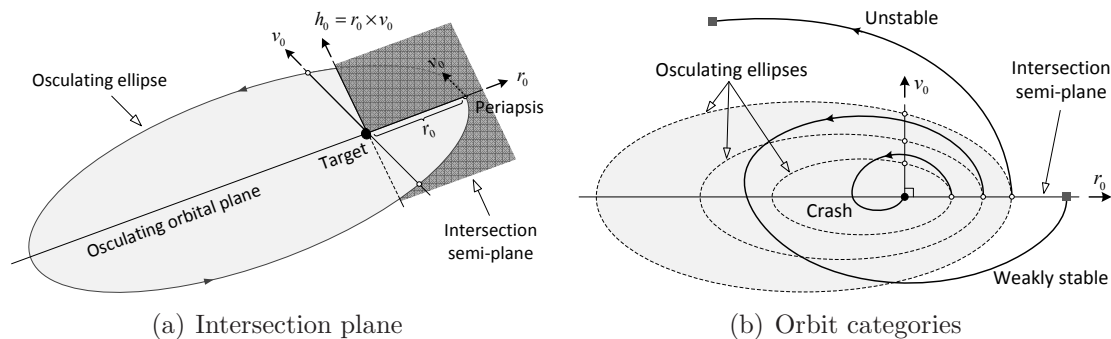
Figure 2: Definition of stability.

The adimensional Kepler energy of the particle with respect to the planet is

$$H(t) = \frac{v^2(t)}{2} - \frac{1}{r(t)}, \tag{5}$$

where $r(t) = \|\mathbf{r}(t)\|$ and $v(t) = \|\mathbf{v}(t)\|$. The function $H(t)$ is not constant due to third-body perturbations. The sign of $H(t)$ gives a clue to which body dominates over the particle trajectory.

Remark 2 (Escape). *The particle escapes from the target at time t_e if the following two conditions are simultaneously satisfied,*

$$H(t_e) > 0, \qquad r(t_e) > R_s, \tag{6}$$

where R_s is the radius of the planet sphere of influence (see Table 1).

The two conditions in (6) have to be satisfied simultaneously because the first one alone does not guarantee escape, and vice versa (Sousa Silva and Terra, 2012). Given $\mathbf{r}_0$, $\mathbf{v}_0$ and an initial epoch t_0, the particle motion is integrated forward under Eqs. (2). Impacts occur at time t_i when $r(t_i) \leq R$, with R as in Table 1. Orbits are classified into four different categories (see Fig. 2(b)).

7

Remark 3 (Orbits classification). *The following sets of initial conditions (i.c.) are constructed according to the orbits they generate.*

1) *Weakly Stable Set, $\mathcal{W}_1$: contains i.c. whose orbits perform a complete revolution about the planet without escaping from or impacting with it (see Fig. 3(a)).*

2) *Unstable Set, $\mathcal{X}_1$: contains i.c. whose orbits escape from the planet without completing any revolution around it (see Fig. 3(b)).*

3) *Crash Set, $\mathcal{K}_1$: contains i.c. whose orbits impact with the planet without completing any revolution around it (see Fig. 3(c)).*

4) *Acrobatic Set, $\mathcal{D}_1$: contains i.c. with orbits not satisfying the above conditions within a given time span of $T = 8\pi (R_s)^{3/2}$ (see Fig. 3(d)).*

(a) Weakly stable   (b) Unstable   (c) Crash   (d) Acrobatic
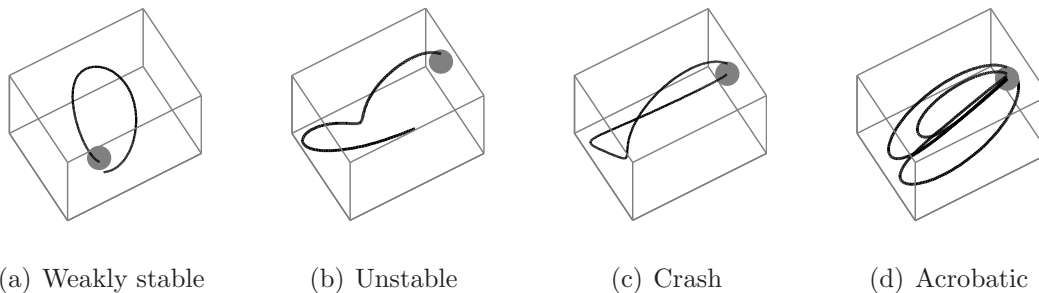
Figure 3: Sample orbits in the EME2000 frame. The grey spot is Mercury (not to scale).

3.2. Step 1: Definition of a Computational Grid

In three-dimensions, an initial condition is specified by six orbital elements. In the analysis below, the particle is initially placed at the periapsis of an osculating ellipse; i.e., the initial true anomaly is zero. This is consistent with the assumptions in Belbruno (2004); García and Gómez (2007); Topputo and Belbruno (2009). Moreover, the initial osculating eccentricity is also fixed. A value of $e_0 = 0.95$ is assumed in this work. Analyses in Circi and Teofilatto (2005); Hyeraci and Topputo (2010); Circi (2012) show that a value of $e_0 \in [0.9, 1)$ is appropriate to support ballistic capture. Thus, four orbital elements are left free. These are the periapsis radius and the argument of periapsis, r_0 and ω_0, respectively, which define the particle position in the initial orbital plane, as well as the inclination and RAAN, i_0 and Ω_0, respectively, which define the initial plane orientation. These initial elements are defined

8

in the RTN@t_0 frame. The initial condition they generate is then converted in the EME2000 frame through (1), where integration is carried out under Eqs. (2) with initial epoch t_0 given.

In Luo et al. (2014), fixed values of i_0 and Ω_0 were taken, while a discretization of r_0 and ω_0 was assumed. This approach is reproduced in this work to show the results in Sections 4.1 and 4.2. The terms r_0 and ω_0 are taken by discretizing $[R + \epsilon, R_s]$ and $[0, 2\pi)$ with N_{r_0} and N_{ω_0} evenly spaced points, respectively ($\epsilon = 1$ km). In the simulations below, $N_{r_0} = 600$ and $N_{\omega_0} = 360$. In Section 4.3, i_0 and Ω_0 are let to vary to assess the influence of the initial plane orientation. These two angles are taken by uniform discretization of $[0, \pi]$ and $[0, 2\pi]$ with $N_{i_0} = 5$ and $N_{\Omega_0} = 8$ points, respectively.

3.3. Step 2: Construction of Ballistic Capture Orbits

The classification in Remark 3 can be applied to orbits performing n revolutions forward in time, $n \geq 1$, and therefore the sets $\mathcal{W}_n$, $\mathcal{X}_n$, $\mathcal{K}_n$, and $\mathcal{D}_n$ can be defined starting from $\mathcal{W}_{n-1}$. Moreover, performing a backward integration yields the sets $\mathcal{W}_{-1}$, $\mathcal{X}_{-1}$, $\mathcal{K}_{-1}$, and $\mathcal{D}_{-1}$. The capture set, a set containing initial conditions that generate ballistic capture orbits, is achieved through

$$\mathcal{C}_{-1}^n = \mathcal{X}_{-1} \cap \mathcal{W}_n. \tag{7}$$

The initial condition in $\mathcal{C}_{-1}^n$ give rise to orbits that 1) escape the planet in backward time ($\mathcal{X}_{-1}$ part), or equivalently approach it in forward time from outside of the SOI, and 2) perform at least n revolutions about the planet ($\mathcal{W}_n$ part). The backward and forward orbits are linked at t_0 where they share the initial state defined by the osculating orbital parameters. A value of $n = 6$ is taken in this work. The reader can refer to Hyeraci and Topputo (2010); Luo et al. (2014) for more details.

3.4. Step 3: Ranking of Candidate Orbits

The capture set defined in (7) contains a number of points that depend upon the discretization with which $\mathcal{W}_n$ and $\mathcal{X}_{-1}$ are computed. A fine discretization is usually favored not to lose possible interesting dynamics, although this generates numerous spurious solutions in $\mathcal{C}_{-1}^n$. The focus is on those ideal orbits having a regular post-capture behavior. A stability index is introduced in Luo et al. (2014) with the purpose of ranking the solutions in the capture sets in terms of their quality. This reads

$$\mathcal{S} = \frac{t_n - t_0}{n}, \tag{8}$$

where t_n is the time at which the n-th revolution is completed.

9

Physically, the value of $\mathcal{S}$ represents the mean period of the post-capture portion. For a Keplerian elliptic orbit, $\mathcal{S}_k = 2\pi[r_0/(1 - e_0)]^{3/2}$. Numerical experiments show that low values of $\mathcal{S}$ are associated to regular post capture orbits, which are desirable. Therefore, orbits are ranked in terms of their stability index, from lowest to highest. In Fig. 4, the points in the capture set $\mathcal{C}_{-1}^6$ about Mercury are shown together with their stability index. The orbits corresponding to two sample solutions (those indicated with arrows in Fig. 4(b)) are presented in Fig. 5.

(a) Capture set, $\mathcal{C}_{-1}^6$
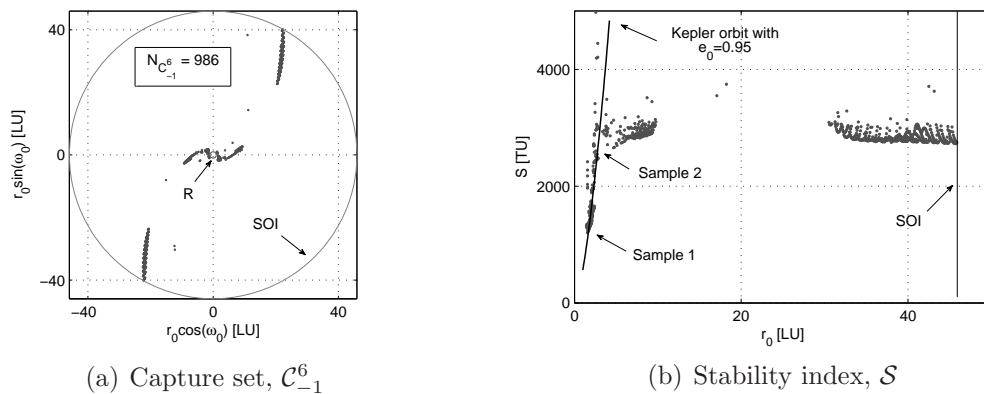
(b) Stability index, $\mathcal{S}$

Figure 4: Points in the capture set $\mathcal{C}_{-1}^6$ about Mercury and their stability index ($\mathcal{S}_k$ superimposed for comparison); $e_0 = 0.95$, $i_0 = \pi/4$, $\Omega_0 = 3\pi/4$, and $t_0 = 2458891.70$ JD.

(a) Sample orbit 1, $\mathcal{S} = 1,204$ TU

(b) Sample orbit 2, $\mathcal{S} = 2,695$ TU
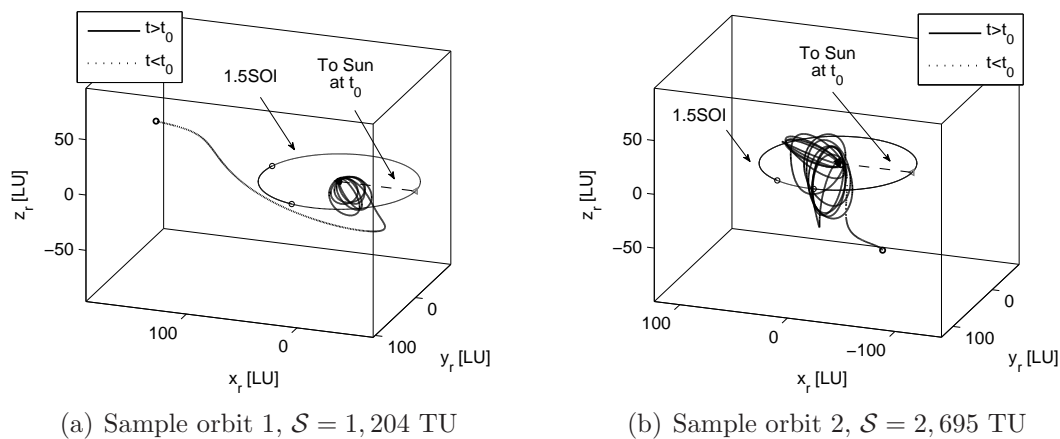
Figure 5: Sample orbits in the RTN@t_0 frame centered at Mercury.

To measure the occurrence of capture orbits in the total set of initial conditions,

10

the capture ratio is defined,

$$\mathcal{R}_c = \frac{N_{\mathcal{C}^6_{-1}}}{N_{r_0} \times N_{\omega_0}},\qquad(9)$$

where $N_{\mathcal{C}^n_{-1}}$ is the number of points in $\mathcal{C}^6_{-1}$. The capture ratio is computed for specific values of i_0 and Ω_0. The value of $\mathcal{R}_c$ indicates how easily a particle can be captured by the target under the parameters of the simulation. While $\mathcal{S}$ is a qualitative index, $\mathcal{R}_c$ is a quantitative measure for the capture solutions.

4. Analysis and Discussion
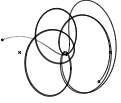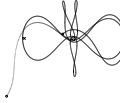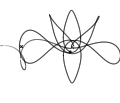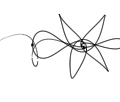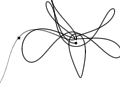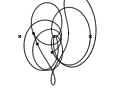
4.1. The Role of Planet's Eccentricity

In this section we compare the results of simulations carried out in the CRTBP, ERTBP, and EPHE models. Without any loss of generality, i_0 is set to 0; i.e., the initial osculating ellipse is assumed in the mutual orbital plane of the Sun and the planet; correspondingly, Ω_0 is not defined. At t_0, the planet is located at perihelion when using the ERTBP and the EPHE models. For each simulation, the capture ratio, $\mathcal{R}_c$, and the minimum stability index, $\mathcal{S}_{\min}$, are computed. The latter is the minimum value in TU of $\mathcal{S}$ in (8) computed for all of the orbits in $\mathcal{C}^6_{-1}$. The results of the simulations are summarized in Table 3.

By inspection of Table 3 it can be seen that $\mathcal{R}_c$ increases when going from the CRTBP to the ERTBP (except for Jupiter, which may be due to the specific parameters of the simulation). Therefore, the capture sets constructed in the elliptic problem are, in general, larger than those in the circular model. This extends the observation in Hyeraci and Topputo (2010) for the Sun–Mercury system. Moreover, there is a good agreement between ERTBP and EPHE, except for Jupiter and Saturn, where the mutual fourth-body perturbations are relevant.

By looking at the orbits in Table 3, it can be seen that orbits in the CRTBP differ significantly from those in the ERTBP. This difference is enhanced for increasing planetary eccentricity, so making the CRTBP inadequate in systems with non-negligible eccentricity (e.g., Sun–Mercury and Sun–Mars, see Table 1). A similar conclusion is provided in Makó and Szenkovits (2004). Moreover, by comparing the capture ratio across different elliptic Sun–planet systems it can be seen that $\mathcal{R}_c$ increases for increasing planetary eccentricity. Figure 6 reports the trend found in the simulations conducted. The linear trend indicates that higher planetary eccentricities ease the ballistic capture occurrence. This is valid within the assumption of these simulations (planet at perihelion at initial time) and can be explained by studying the dynamics of the zero velocity curves (Circi and Teofilatto, 2005;

11

Table 3: Capture ratios and minimum stability indices for $\mathcal{C}_{-1}^6$ in different systems and with different models. Orbits corresponding to $\mathcal{S}_{\min}$ are shown in the BPR frame.

System	Model	Mercury	Venus	Earth	Mars	Jupiter	Saturn
	CRTBP	0.020	0.118	0.148	0.203	0.311	0.182
$\mathcal{R}_c$ (‰)	ERTBP	0.907	0.128	0.161	0.295	0.207	0.223
	EPHE	0.907	0.128	0.160	0.315	0.225	0.264
	CRTBP	3,037	7,367	9,277	15,180	56,809	77,823
$\mathcal{S}_{\min}$ (TU)	ERTBP	1,248	7,321	7,837	10,143	38,421	71,065
	EPHE	1,248	7,229	7,837	10,143	38,748	70,991
	CRTBP						
Orbit ($\mathcal{S}_{\min}$)	ERTBP						
	EPHE.						

Hyeraci and Topputo, 2013). More complete analyses with variable true anomaly are conducted later.
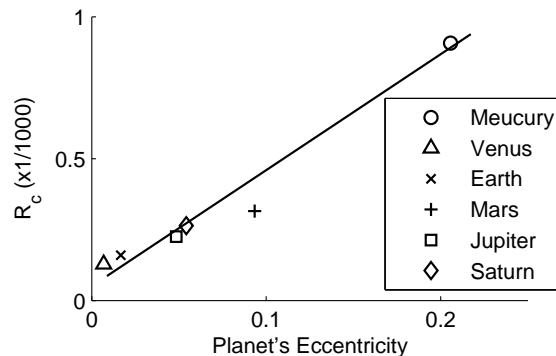
Figure 6: Capture ratio versus planetary eccentricity. A trendline is superimposed for reference.

For given Sun–planet system, the value of $\mathcal{S}_{\min}$ decreases when going from the CRTBP to the ERTBP, so showing that the planet orbital ellipticity is useful for producing regular, stable post-capture orbits. Table 3 also shows that the elliptic model is an accurate approximation of the real model since the figures and orbits have negligible differences between ERTBP and EPHE.

Result 1 (Role of planet eccentricity). *In the Sun–planets systems, with the planet at perihelion at initial time, the following results are found.*

- *The capture sets computed in the elliptic models are generally larger than those computed in the circular models;*

- *The capture ratio increases for increasing planet eccentricity;*

- *The capture orbits in the elliptic models have lower stability indices than those computed in the circular models.*

4.2. The Role of Planet's True Anomaly

Previous studies have shown that the ballistic capture dynamics depends upon the position of the planet along its orbit, or its true anomaly f. Desirable conditions for capture occur when the particle is in Lagrange point region and, at the same time, the planet is at perihelion (Circi, 2012) or, equivalently, the particle is at the closest approach and the planet has $f = \pi/4$ (Hyeraci and Topputo, 2013). However, it is not clear if the maximum $\mathcal{R}_c$ and minimum $\mathcal{S}$ conditions occur simultaneously, and the way prograde and retrograde orbits behave in this perspective.

13

In this section we conduct an analysis with the same settings as in Section 4.1 except for the initial true anomaly of the planet, which is allowed to vary within $[0, 2\pi]$ with steps of $\pi/4$, and the initial inclination, i_0, which is either 0 (planar prograde orbits) or π (planar retrograde orbits). The ERTBP is chosen for these simulations due to the high fidelity shown in Section 4.1.

The variation of $\mathcal{R}_c$ with f for both prograde and retrograde orbits in the various Sun–planet systems is shown in Fig. 7. To ease the cross-comparisons among different systems, the y-axis reports the normalized capture ratio $\mathcal{R}_c/\min(\mathcal{R}_c)$, where $\min(\mathcal{R}_c)$ is the minimum capture ratio of each Sun–planet system. The true anomalies corresponding to maximum $\mathcal{R}_c$ for each planet are outlined in Fig. 8(a).

(a) Planar prograde (b) Planar retrograde
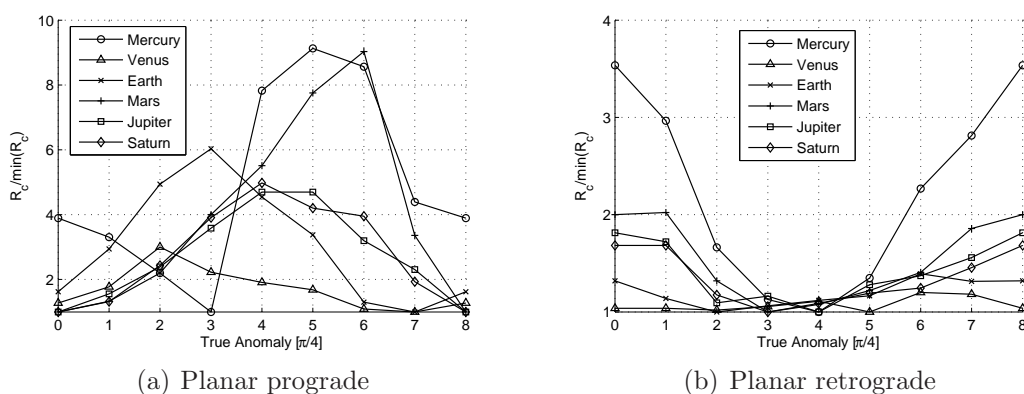
Figure 7: Normalized capture ratio versus true anomaly.

(a) Maximum $\mathcal{R}_c$ vs true anomaly (b) Minimum $\mathcal{S}_{\min}$ vs true anomaly
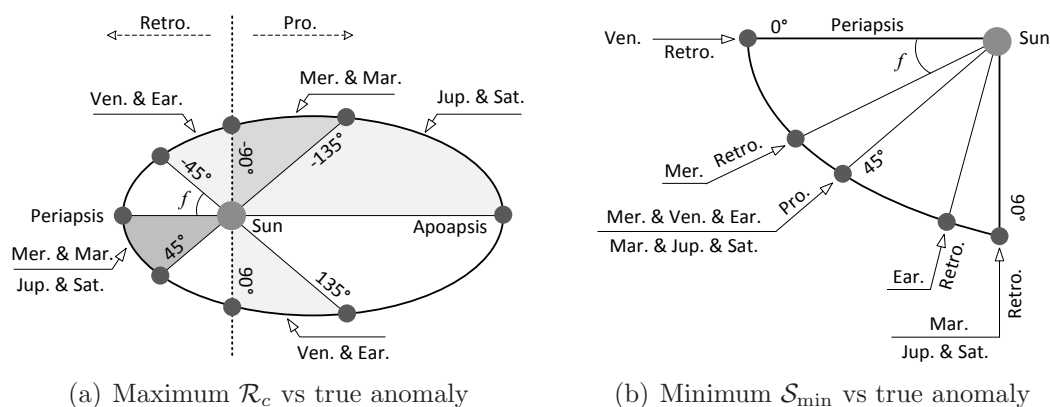
Figure 8: True anomalies of maximum $\mathcal{R}_c$ and minimum $\mathcal{S}_{\min}$.

From inspection of Figs. 7 and 8(a), the following can be said. 1) When the

quantity of capture orbits is of interest, the true anomaly at which their number is maximum is neither $f = 0$ nor $f = \pi/4$. 2) The true anomalies associated to maximum capture ratio for prograde orbits (II and III quadrant) are in opposition to those of the retrograde orbits (I and IV quadrant); note that $f \simeq 5/4\pi - 3/2\pi$ for Mercury prograde orbits is consistent with the results in Hyeraci and Topputo (2013). 3) The variation of capture probability with f increases with planet orbital eccentricity; e.g., for Mercury prograde case, the maximum $\mathcal{R}_c$ is 9 times the minimum $\mathcal{R}_c$. 4) The inclination has a significant influence on the distribution of the capture ratios; for instance, the maximum capture ratios for prograde orbits are almost 3 times those of retrograde orbits. The values of maximum $\mathcal{R}_c$ for both prograde and retrograde orbits are given in Tables 4 and 5, respectively.

Table 4: Maximum $\mathcal{R}_c$ and minimum $\mathcal{S}_{\min}$ for varying true anomaly (prograde orbits, ERTBP).
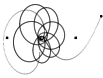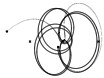
Parameter	Mercury	Venus	Earth	Mars	Jupiter	Saturn
max $\mathcal{R}_c$ (‰)	2.128	0.300	0.601	2.666	0.974	1.110
min $\mathcal{S}_{\min}$ (TU)	1,115	6,283	7,634	9,923	36,689	70,229
Orbit ($\mathcal{S}_{\min}$)						

Table 5: Maximum $\mathcal{R}_c$ and minimum $\mathcal{S}_{\min}$ for varying true anomaly (retrograde orbits, ERTBP).

Parameter	Mercury	Venus	Earth	Mars	Jupiter	Saturn
max $\mathcal{R}_c$ (‰)	1.541	0.301	0.408	0.890	0.449	0.487
min $\mathcal{S}_{\min}$ (TU)	1,588	6,479	8,266	12,129	42,968	75,803
Orbit ($\mathcal{S}_{\min}$)						

The analysis conducted for what concerns the stability index is summarized in Fig. 9 and outlined also in Fig. 8(b). Not surprisingly, these results show that ideal orbits (i.e., those with lowest $\mathcal{S}_{\min}$) exist in the range $f \in [0, \pi/2]$, no matter for prograde or retrograde. This result is in good agreement with that in Hyeraci and Topputo

15
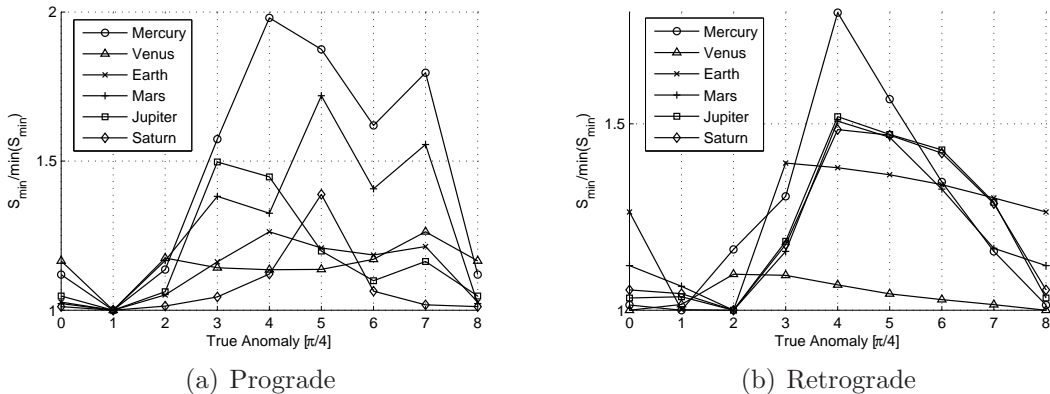
Figure 9: Stability index $\mathcal{S}_{\min}$ vs true anomaly f.

(2013), obtained by studying the dynamics of the zero-velocity curves in the ERTBP. More precisely, for prograde orbits the minimum $\mathcal{S}_{\min}$ is located at $f = \pi/4$ for all the cases considered; for retrograde orbits, this minimum is located in the range $f \in [\pi/4, \pi/2]$, besides the case of Venus that presents an almost regular trend (this is due to its small eccentricity, see Table 1). The minimum $\mathcal{S}_{\min}$ for these simulations is presented in Tables 4 and 5. Apparently, the post-capture legs of prograde motions are more regular than the retrograde motions.

In summary, we have the following.

Result 2 (Role of true anomaly). *In the Sun–planet systems, when their true anomaly is allowed to vary, the following is observed.*

- *The capture sets are bigger when f is in the II or III quadrant for prograde orbits, and in the I or IV quadrant for retrograde orbits;*

- *The stability index is minimum when f is in the I quadrant for both prograde and retrograde orbits.*

4.3. The Role of Particle Inclination and Orientation

In this section we complete the analyses in the previous sections by investigating how the out-of-plane motion affects the ballistic capture dynamics. This case is not fully addressed in literature. In Romagnoli and Circi (2009); Makó et al. (2010); Makó (2014), a spatial definition of capture is given with the aid of two angles; the effects of these two angles is analyzed in the Earth–Moon and Sun–Mercury systems, respectively. In this paper, we investigate the role of the osculating initial inclination

16

(i_0) and orientation (Ω_0) by using the spatial stability defined in Section 3.1. Without any loss of generality, the initial true anomaly is set to 0, whereas both i_0, Ω_0 are discretized with steps of 0.25π. The ERTBP is used for numerical integrations. The capture ratio trend for different i_0 and Ω_0 is presented in Fig. 10. Note that the contours here and hereafter are generated by a two dimensional interpolation.
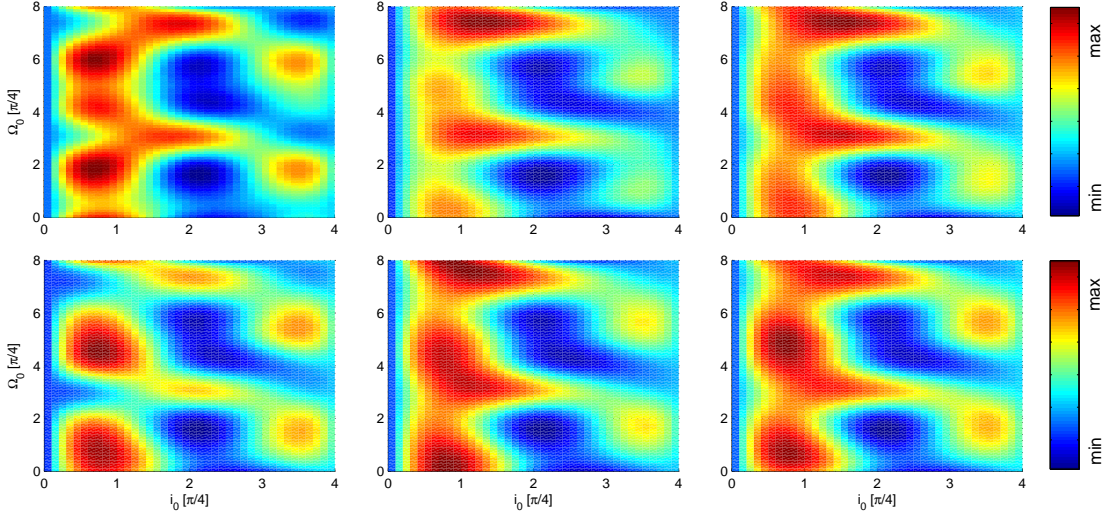

Figure 10: Capture ratio $\mathcal{R}_c$ for varying i_0 and Ω_0. From left to right, top to bottom: Mercury, Venus, Earth, Mars, Jupiter, Saturn.

Surprisingly, the regions with largest capture probability are not located about the Sun–planet plane, i.e., at neither $i_0 \simeq 0$ nor $i_0 \simeq \pi$. Instead, the maxima $\mathcal{R}_c$ lie at some non-zero inclination: at $i_0 \simeq 40 - 70$ deg for different Sun–planet systems, depending on Ω_0. Besides, a second peak appears at $i_0 \simeq 150 - 160$ deg (retrograde orbits). This result is analogous to that in Neto and Winter (2001), in which the largest probability with the longest capture times was found at inclinations of $60-70$ deg and 160 deg in the Sun–Uranus system. This correspondence confirms the results of the present work and extends those in Neto and Winter (2001) to the Sun–planet cases. From a global point of view, a quasi-symmetry in RAAN exists, e.g., $\Omega_0 \rightarrow \Omega_0 + \pi$. This is also observed in Belbruno (2004); García and Gómez (2007); Topputo and Belbruno (2009); Romagnoli and Circi (2009); Makó et al. (2010); Luo et al. (2014) and is due to the properties of the stable sets. By cross-comparing the plots in Fig. 10, it is found that the spatial distributions of $\mathcal{R}_c$ is similar, regardless of planets eccentricity and mass ratio. The values of maximum capture ratio for each system are reported in Table 6. Comparisons with Table 3 show a notable increase

17

in $\mathcal{R}_c$ when extending to spatial initial conditions.

Table 6: Maximum capture ratio and minimum stability index when the initial inclination and orientation vary ($e_0 = 0.95$; ERTBP).

Parameter	Mercury	Venus	Earth	Mars	Jupiter	Saturn
max $\mathcal{R}_c$ (‰)	6.341	1.498	1.404	2.797	1.763	1.587
min $\mathcal{S}_{\min}$ (TU)	1,204	4,419	7,249	10,143	38,421	67,179
Orbit (BPR)						

Similarly, Fig. 11 shows the trend of $\mathcal{S}_{\min}$ with respect to i_0 and Ω_0, whereas Table 6 reports the values of minimum $\mathcal{S}_{\min}$ and its associated orbits. Two points are concluded: 1) the prograde orbits ($i_0 \leq 90$ deg) have in general a more regular (less $\mathcal{S}_{\min}$) post-capture leg than the retrograde orbit ($i_0 \geq 90$ deg); 2) the value of $\mathcal{S}_{\min}$ is susceptible to Ω_0, particularly when $i = 90$ deg (initial polar orbits). By comparing Fig. 10 and 11, it can be seen that the regions with maximum $\mathcal{R}_c$ are in agreement with those having minimum $\mathcal{S}_{\min}$. That is to say, the (i_0, Ω_0) plane that produces the most regular capture orbits is also the one that maximizes the chances of capture. This is a deep result.

Result 3 (Role of plane orientation). *In the Sun–planets systems, with the planet at perihelion at initial time, when the initial inclination and orientation of the particle are let to vary, the following is observed.*

- *The maximum chance of capture does not occur in the Sun–planet plane;*

- *There are two different inclination ranges where the capture ratio is maximum;*

- *Prograde orbits produce more regular post-capture dynamics;*

- *The minimum stability index depends on the initial orientation, especially for polar orbits.*

5. Conclusion

This paper treats the ballistic capture dynamics in six Sun–planet systems by using a construction method developed in previous works. Effort has been put to
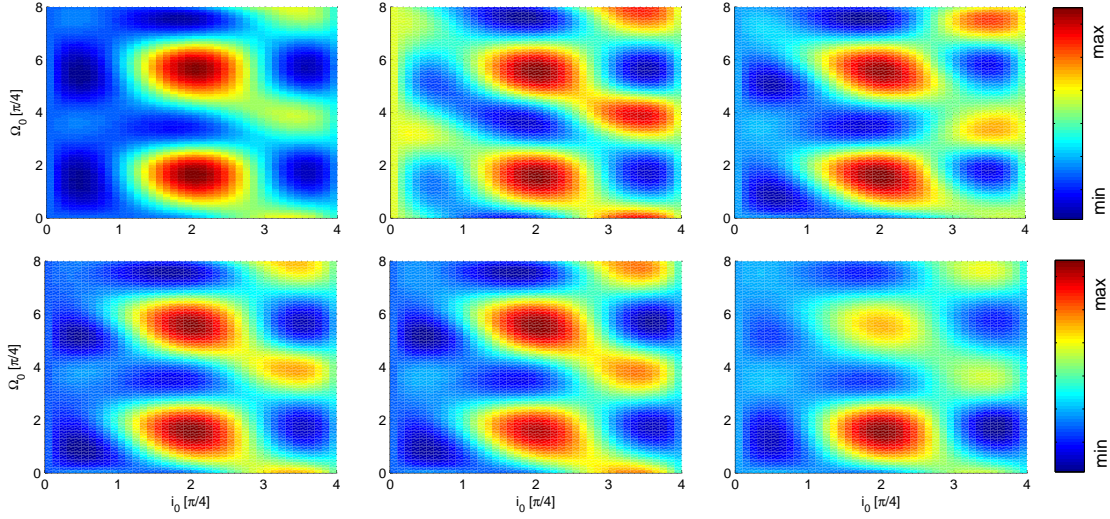
18

Figure 11: Minimum stability index $\mathcal{S}_{\min}$ for varying i_0 and Ω_0. From left to right, top to bottom: Mercury, Venus, Earth, Mars, Jupiter, Saturn.

assess the role played by the dynamical model, the planetary true anomaly and eccentricity, as well as the particle initial plane. In brief, the following has been found.

1) The CRTBP is not adequate for constructing ballistic capture orbits; the elliptic problem generates a higher probability of capture orbits than the circular one; the larger the planetary eccentricity is, the easier the particle can be ballistically captured; the ERTBP is a good approximation of the real model.

2) A configuration with the planet at aphelion maximizes the chances of capture for prograde orbits; conversely, the planet at perihelion favors capture of retrograde orbits; prograde orbits are, in general, captured more easily than retrograde orbits; a planet true anomaly in the range $\pi/4 - \pi/2$ generates regular post-capture orbits.

3) The spatial distribution has significant effect on the capture dynamics; inclinations in the range $40 - 70$ deg and $150 - 160$ deg promote capture and regularity; capture dynamics is sensitive to RAAN; initial planes that maximize the chances of capture are also those that produce regular post-capture orbits.

As a general remark, we can say that ballistic capture is an interesting phenomenon that is not fully understood. It requires additional, in-depth studies.

Acknowledgements

References

Alessi, E.M., Pergola, P., 2012. Two options for the callisto's exploration. Acta Astronautica 72, 185 – 197. doi:10.1016/j.actaastro.2011.09.003.

Astakhov, S.A., Burbanks, A.D., Wiggins, S., Farrelly, D., 2003. Chaos-assisted capture of irregular moons. Nature 423, 264–267. doi:10.1038/nature01622.

Belbruno, E., 2004. Capture Dynamics and Chaotic Motions in Celestial Mechanics: With Applications to the Construction of Low Energy Transfers. Princeton University Press.

Belbruno, E., Miller, J., 1993. Sun-Perturbed Earth-to-Moon Transfers with Ballistic Capture. Journal of Guidance, Control, and Dynamics 16, 770–775. doi:10.2514/3.21079.

Brasil, P., Prado, A., Deienno, R., Yokoyama, T., 2015. Study of the gravitational capture of a spacecraft by Jupiter. Advances in Space Research 55, 668–681. doi:10.1016/j.asr.2014.11.005.

Brunini, A., 1996. On the satellite capture problem: capture and stability regions for planetary satellites. Celestial Mechanics and Dynamical Astronomy 64, 79–92.

Campagnola, S., Buffington, B., Petropoulos, A., 2014. Jovian Tour Design for Orbiter and Lander Missions to Europa. Acta Astronautica 100, 68–81. doi:10.1016/j.actaastro.2014.02.005.

Chung, M.J., Hatch, S.J., Kangas, J.A., Long, S.M., Roncoli, R.B., Sweetser, T.H., 2010. Trans-Lunar Cruise Trajectory Design of GRAIL (Gravity Recovery and Interior Laboratory) Mission, in: AIAA/AAS Astrodynamics Specialist Conference, AIAA 2010-8384, Toronto, Ontario, Canada. pp. 2–5.

Circi, C., 2012. Properties of Transit Trajectory in the Restricted Three and Four-Body Problem. Advances in Space Research 49, 1506–1519. doi:10.1016/j.asr.2012.02.034.

Circi, C., Teofilatto, P., 2005. Effect of Planetary Eccentricity on Ballistic Capture in the Solar System. Celestial Mechanics and Dynamical Astronomy 93, 69–86. doi:10.1007/s10569-005-3640-9.

Conley, C.C., 1968. Low Energy Transit Orbits in the Restricted Three-Body Problem. SIAM Journal on Applied Mathematics 16, 732–746. doi:10.1137/0116060.

Elliot, J., Alkalai, L., 2011. Lunette: A Network of Lunar Landers for In-Situ Geophysical Science. Acta Astronautica 68, 1201–1207. doi:10.1016/j.actaastro.2010.10.024.

Folkner, W.M., Williams, J.G., Boggs, D.H., Park, R.S., Kuchynka, P., 2014. The Planetary and Lunar Ephemerides DE430 and DE431. Technical Report. IPN Progress Report 42-196.

García, F., Gómez, G., 2007. A Note on Weak Stability Boundaries. Celestial Mechanics and Dynamical Astronomy 97, 87–100. doi:10.1007/s10569-006-9053-6.

Gómez, G., Koon, W.S., Lo, M.W., Marsden, J.E., Masdemont, J., Ross, S.D., 2001. Invariant Manifolds, the Spatial Three-Body Problem and Space Mission Design. Advances in the Astronautical Sciences 109, 3–22.

Hyeraci, N., Topputo, F., 2010. Method to design ballistic capture in the elliptic restricted three-body problem. Journal of Guidance, Control, and Dynamics 33, 1814–1823. doi:10.2514/1.49263.

Hyeraci, N., Topputo, F., 2013. The role of true anomaly in ballistic capture. Celestial Mechanics and Dynamical Astronomy 116, 175–193. doi:10.1007/s10569-013-9481-z.

Jehn, R., Campagnola, S., García, D., Kemble, S., 2004. Low-Thrust Approach and Gravitational Capture at Mercury, in: Proceedings of the 18th International Symposium on Space Flights Dynamics, Munich, Germany. p. 487.

Koon, W.S., Lo, M.W., Marsden, J.E., Ross, S.D., 2001. Low Energy Transfer to the Moon. Celestial Mechanics and Dynamical Astronomy 81, 63–73. doi:10.1023/A:1013359120468.

Lee, E.A., Astakhov, S.A., Farrelly, D., 2007. Production of trans-neptunian binaries through chaos-assisted capture. Mon. Not. R. Astron. Soc. 379, 229–246. doi:10.1111/j.1365-2966.2007.11930.x.

Lei, H., Xu, B., Sun, Y., 2013. Earth-moon low energy trajectory optimization in the real system. Advances in Space Research 51, 917–929. doi:10.1016/j.asr.2012.10.011.

Luo, Z.F., Topputo, F., Bernelli-Zazzera, F., Tang, G.J., 2014. Constructing Ballistic Capture Orbits in the Real Solar System Model. Celestial Mechanics and Dynamical Astronomy 120, 433–450. doi:10.1007/s10569-014-9580-5.

Machuy, A.L., Prado, A.F.B.A., Stuchi, T.J., 2007. Numerical study of the time required for the gravitational capture in the bi-circular four-body problem. Advances in Space Research 40, 118–124.

Makó, Z., 2014. Connection between Hill Stability and Weak Stability in the Elliptic Restricted Three-Body Problem. Celestial Mechanics and Dynamical Astronomy In press, 1–16. doi:10.1007/s10569-014-9577-0.

Makó, Z., Szenkovits, F., 2004. Capture in the Circular and Elliptic Restricted Three-Body Problem. Celestial Mechanics and Dynamical Astronomy 90, 51–58. doi:10.1007/s10569-004-5899-7.

Makó, Z., Szenkovits, F., Salamon, J., Oláh-Gál, R., 2010. Stable and Unstable Orbits around Mercury. Celestial Mechanics and Dynamical Astronomy 108, 357–370. doi:10.1007/s10569-010-9309-z.

Neto, E.V., Winter, O.C., 2001. Time analysis for temporary gravitational capture: Satellites of uranus. The Astronomical Journal 122, 440–448.

Prado, A., Neto, E.V., 2006. Study of the gravitational capture in the elliptical restricted three-body problem. The Journal of the Astronautical Sciences 54, 567–582. doi:10.1007/BF03256506.

Romagnoli, D., Circi, C., 2009. Earth–Moon Weak Stability Boundaries in the Restricted Three and Four Body Problem. Celestial Mechanics and Dynamical Astronomy 103, 79–103. doi:10.1007/s10569-008-9169-y.

Russell, R.P., 2012. Survey of Spacecraft Trajectory Design in Strongly Perturbed Environments. Journal of Guidance, Control, and Dynamics 35, 705–720. doi:10.2514/1.56813.

Schoenmaekers, J., Horas, D., Pulido, J.A., 2001. SMART-1: With Solar Electric Propulsion to the Moon, in: Proceeding of the 16th International Symposium on Space Flight Dynamics, Pasadena, California. pp. 3–7.

Sousa Silva, P., Terra, M., 2012. Applicability and Dynamical Characterization of the Associated Sets of the Algorithmic Weak Stability Boundary in the Lunar Sphere of Influence. Celestial Mechanics and Dynamical Astronomy 113, 141–168. doi:10.1007/s10569-012-9409-z.

Szebehely, V., 1967. Theory of Orbits: The Restricted Problem of Three Bodies. Academic Press Inc.

Topputo, F., 2013. On Optimal Two-Impulse Earth-Moon Transfers in a Four-Body Model. Celestial Mechanics and Dynamical Astronomy 117, 279–313. doi:10.1007/s10569-013-9513-8.

Topputo, F., Belbruno, E., 2009. Computation of Weak Stability Boundaries: Sun–Jupiter System. Celestial Mechanics and Dynamical Astronomy 105, 3–17. doi:10.1007/s10569-009-9222-5.

Topputo, F., Belbruno, E., 2015. Earth–Mars Transfers with Ballistic Capture. Celestial Mechanics and Dynamical Astronomy 121, 329–346. doi:10.1007/s10569-015-9605-8.

Urrutxua, H., Scheeres, D., Bombardelli, C., Gonzalo, J., Pelaez, J., 2014. What Does it Take to Capture an Asteroid? A Case Study on Capturing Asteroid 2006 RH120, in: 24th AAS/AIAA Space Flight Mechanics Meeting, Santa Fe, New Mexico, 26–30 January, pp. 1–20.

Vetrisano, M., Van der Weg, W., Vasile, M., 2012. Navigating to the moon along low-energy transfers. Celestial Mechanics and Dynamical Astronomy 114, 25–53. doi:10.1007/s10569-012-9436-9.

Yamato, H., Spencer, D., 2004. Transit-orbit search for planar restricted three-body problems with perturbations. Journal of Guidance, Control, and Dynamics 27, 1035–1045.